

Nexus-INR: Diverse Knowledge-guided Arbitrary-Scale Multimodal Medical Image Super-Resolution

Bo Zhang¹, Jianfei Huo¹, Zheng Zhang², Wufan Wang¹, Hui Gao³, Xiyang Gong¹, Wendong Wang¹

¹ State Key Laboratory of Networking and Switching Technology, School of Computer Science (National Pilot Software Engineering School), Beijing University of Posts and Telecommunications.

² School of Intelligent Engineering and Automation, Beijing University of Posts and Telecommunications.

³ School of Computer Science (National Pilot Software Engineering School), Beijing University of Posts and Telecommunications.

zbo@bupt.edu.cn, jfhuo@bupt.edu.cn, zhangzheng@bupt.edu.cn, wufanwang@bupt.edu.cn, gaohui786@bupt.edu.cn, xygong@bupt.edu.cn, wdwang@bupt.edu.cn

Abstract

Arbitrary-resolution super-resolution (ARSR) provides crucial flexibility for medical image analysis by adapting to diverse spatial resolutions. However, traditional CNN-based methods are inherently ill-suited for ARSR, as they are typically designed for fixed upsampling factors. While INR-based methods overcome this limitation, they still struggle to effectively process and leverage multi-modal images with varying resolutions and details. In this paper, we propose Nexus-INR, a Diverse Knowledge-guided ARSR framework, which employs varied information and downstream tasks to achieve high-quality, adaptive-resolution medical image super-resolution. Specifically, Nexus-INR contains three key components. A dual-branch encoder with an auxiliary classification task to effectively disentangle shared anatomical structures and modality-specific features; a knowledge distillation module using cross-modal attention that guides low-resolution modality reconstruction with high-resolution reference, enhanced by self-supervised consistency loss; an integrated segmentation module that embeds anatomical semantics to improve both reconstruction quality and downstream segmentation performance. Experiments on the BraTS2020 dataset for both super-resolution and downstream segmentation demonstrate that Nexus-INR outperforms state-of-the-art methods across various metrics.

1 Introduction

Traditional convolutional neural networks (CNNs) based super-resolution (SR) methods have achieved remarkable progress in medical super-resolution to facilitate downstream analysis, visualization, and quantitative assessment (Chen et al. 2018; Du et al. 2020a; Pham et al. 2017). Nevertheless, these approaches are typically designed for fixed integer upsampling factors and predefined output grids, making them inflexible for arbitrary-resolution super-resolution (ARSR) (Sitzmann et al. 2020; Tancik et al. 2020; Cao et al. 2023) tasks.

Implicit neural representation (INR) based methods have recently emerged as a promising solution for ARSR. By modeling images as continuous functions that map spatial coordinates to intensities, INR-based methods enable seamless prediction at any desired resolution or spatial grid. This

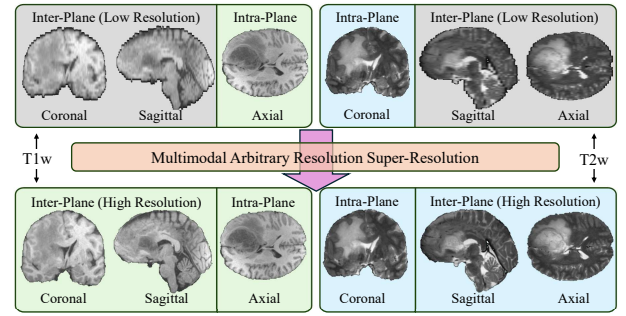


Figure 1: Schematic of multi-modal MRI acquisition. Each modality (e.g., T1w and T2w) can have a different intra-plane (scanning) direction (arrows), with high in-plane resolution and low through-plane resolution. T1w images may have higher resolution than T2w images. The slice orientation and resolution anisotropy of each modality lead to cross-modal heterogeneity.

flexibility allows for adaptation to arbitrary, anisotropic, and non-uniform data, which is highly desirable in practical scenarios. However, current INR-based methods are usually tailored for single-modal or isotropic data, lacking the ability to generalize and fully exploit multi-modal information (McGinnis et al. 2023; Chen, Liu, and Wang 2021; Fang et al. 2024).

However, multimodal MRI has been widely used in modern medical examinations to capture details of organs and tumor tissues (Lyu et al. 2020; Feng et al. 2021; Chen et al. 2025; Wang et al. 2023). As shown in Fig. 1, different modalities are frequently acquired with varying orientations, degrees of anisotropy (e.g., high in-plane but low through-plane resolution), and native resolutions—factors driven by scan time, protocol, and hardware limitations. For example, T1-weighted images may have higher spatial resolution than T2-weighted images, and their slice direction is likely to be different. These discrepancies lead to severe spatial heterogeneity, cross-modal misalignment, and resolution inconsistency in the acquired MRI data. Current INR-based ARSR methods often inherit from natural image processing algorithms, meaning they don’t consider or can’t leverage

the rich, complementary information across modalities, usually only addressing single-modality-specific issues. This hinders the full potential of multi-modal MRI, with super-resolution results for low-resolution modalities being particularly unsatisfactory. How to effectively accommodate the diverse characteristics of multi-modal imaging still needs to be explored in depth.

Moreover, the core value of medical images lies in their role in diagnostic tasks, such as tumor detection and classification, where preserving fine texture details is crucial (Xiao et al. 2024; He et al. 2023). Current super-resolution methods for medical images usually focus on improving image fidelity (e.g., PSNR), overlooking diagnostic accuracy (Wang et al. 2020). These traditional visual metrics usually fail to fully evaluate the practical utility of the medical images. For instance, a super-resolution model that excels in PSNR might negatively or even detrimentally impact downstream tasks if it introduces artifacts or distorts details in small lesions. Therefore, medical image super-resolution should strive to improve both clarity and diagnostic accuracy.

To address these issues, we propose Nexus-INR, a Diverse Knowledge-guided ARSR, which systematically incorporates three types of diverse knowledge into a unified architecture, can better utilize complementary information between different modalities for better medical image super-resolution, thus providing more accurate data for downstream tasks. Our main contributions are as follows:

- We propose a Diverse Knowledge-guided ARSR framework that employs varied information and downstream tasks to achieve high-quality, adaptive-resolution medical image super-resolution.
- We design a dedicated module to effectively aggregate complementary information from different modalities and orientations, enabling robust feature representation and reconstruction despite spatial heterogeneity.
- We design a cross-modal knowledge distillation module, which transfers anatomical priors from high-resolution reference modalities to low-resolution target modalities, enriching anatomical details and particularly improving SR performance in challenging modalities.
- We introduce an auxiliary segmentation task to explicitly guide the network in optimizing anatomical consistency and semantic structures, thereby enhancing image interpretation and downstream task performance.

2 Related Work

Image Super-Resolution. Recent years have witnessed significant advances in image super-resolution (SR) for medical imaging. Early deep learning-based approaches, such as SRCNN and its 3D extensions (Pham et al. 2017; Chen et al. 2018), enabled end-to-end mapping from low resolution (LR) to high resolution (HR) images and outperformed traditional interpolation-based techniques. Further improvements were achieved by employing deeper residual networks (Du et al. 2020a) and GAN-based models (Chen et al. 2018), which improved reconstruction of fine anatomical details.

To exploit the complementary information in multi-contrast or multi-modal MRI, several dual-branch, attention-

based, or transformer-based frameworks have been proposed. Methods such as MCSR (Lyu et al. 2020), MINet (Feng et al. 2021), and SANet (Feng et al. 2024) leverage easy-to-acquire reference modalities to guide the super-resolution of more challenging modalities, achieving notable improvements in image quality. However, these approaches often rely on accurate image registration and may be sensitive to cross-modal misalignment. Then feature fusion and alignment mechanisms have been proposed. The DANCE framework uses deformable attention and neighborhood aggregation for robust texture transfer and alignment, performing well even with misregistration (Chen et al. 2025).

In addition, INR-based methods have recently gained attention for medical image SR. These approaches model images as continuous functions of spatial coordinates, enabling arbitrary-scale super-resolution and flexible adaptation to anisotropic data (Fang et al. 2024; McGinnis et al. 2023; Wu et al. 2022). INR-based methods have shown promising results in both single-modal and multi-modal SR tasks.

Implicit Neural Representation. Implicit neural representation (INR) methods can model images as continuous functions mapping spatial coordinates to pixel intensities. Classic INR approaches represent images by directly fitting a neural network to coordinate-value pairs, enabling voxel-wise prediction at arbitrary resolutions (Sitzmann et al. 2020; Tancik et al. 2020). This allows for arbitrary-scale super-resolution and flexible adaptation to diverse spatial grids, which is particularly advantageous in medical imaging SR (Wu et al. 2022; Cao et al. 2023).

However, the simplicity of directly mapping coordinates to intensities often limits the expressive capacity of basic INRs, especially when modeling complex anatomical structures or generalizing across subjects and modalities. For example, single-subject INR models are typically restricted to fitting a specific image or single subject, and struggle to generalize or transfer to new cases (McGinnis et al. 2023).

Then various strategies have been proposed to enhance the representational power and generalization ability of INR-based frameworks. One common approach is to incorporate deep features extracted by an encoder, either by concatenating them with spatial coordinates or by using them as conditioning information for the implicit function (Chen, Liu, and Wang 2021; Cao et al. 2023). Meta-learning methods and transformer-based hyper-networks have been developed to provide strong priors or to directly generate the weights of the INR for a new signal, resulting in faster convergence and improved performance with limited observations (Tancik et al. 2021; Chen and Wang 2022). Other works introduce semantic or anatomical priors, such as semantic segmentation maps or attention-based mechanisms, to guide the network in capturing both local and non-local features (Ekanayake et al. 2025; Cao et al. 2023).

The inherent support for ARSR remains a key advantage of INR-based methods, facilitating flexible, memory-efficient, and high-fidelity image reconstruction in both in-scale and out-of-scale scenarios (Wu et al. 2022; Cao et al. 2023; Fang et al. 2024). With ongoing advances in feature conditioning, meta-learning, transformer-based architectures, and attention modeling, INR frameworks are show-

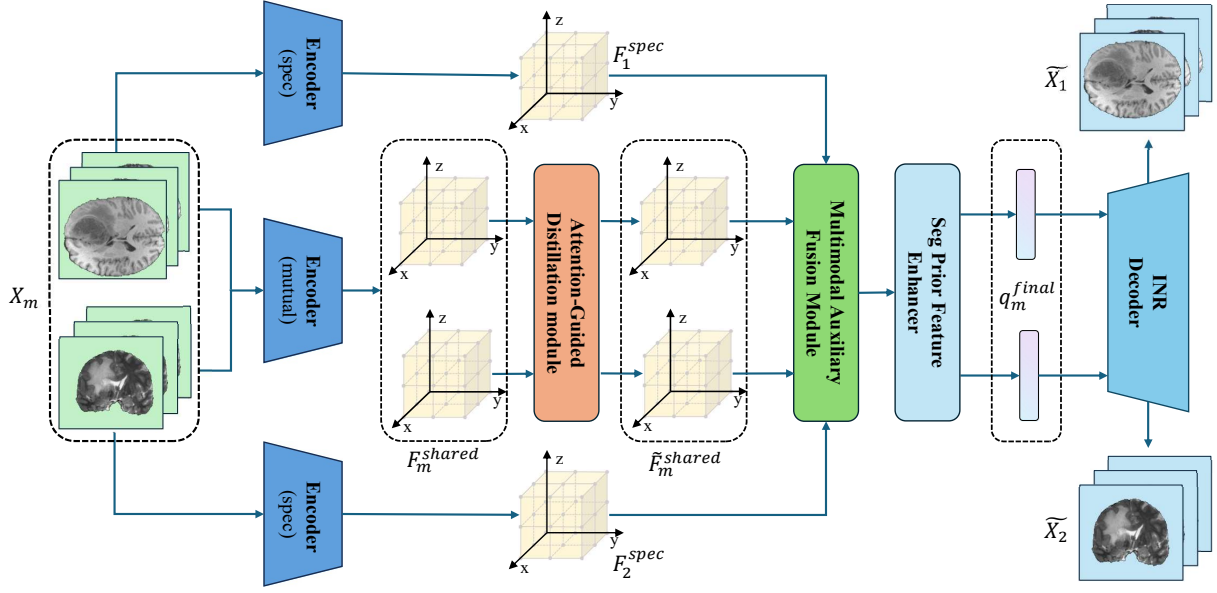


Figure 2: Overview of the Nexus-INR framework. The model consists of dual-branch encoders, cross-modal attention, feature fusion, segmentation enhancement, and a coordinate-based implicit decoder.

ing increasing potential for a broad range of medical image super-resolution tasks.

3 Method

3.1 Problem Formulation

Given a pair of multi-modal MRI volumes, our goal is to reconstruct a high-resolution (HR) image of a target modality from its low-resolution (LR) version, guided by a reference modality. The reference modality is also super-resolved to higher resolution. Let $\mathbf{X}_1 \in \mathbb{R}^{1 \times D_1 \times H_1 \times W_1}$ and $\mathbf{X}_2 \in \mathbb{R}^{1 \times D_2 \times H_2 \times W_2}$ denote two MRI modalities with possibly anisotropic resolutions, and let $\Omega_{\text{HR}} = \{\mathbf{p}\}$ be the desired HR grid. We aim to learn a continuous implicit function f_θ parameterized by deep networks:

$$\hat{y}_m(\mathbf{p}) = f_\theta(\mathbf{X}_1, \mathbf{X}_2, \mathbf{p}), \quad (1)$$

3.2 Overview Framework

The overall architecture of Nexus-INR is shown in Figure 2. Nexus-INR achieves ARSR for multi-modal MRI by leveraging diverse knowledge from different modalities, anatomical priors, and auxiliary tasks such as segmentation. These knowledge sources are processed through separate branches, each focusing on a specific aspect of the information.

To integrate this diverse knowledge, Nexus-INR extracts features from MRI volumes with anisotropic and mismatched resolutions via parallel encoders, aligns them to a unified HR grid, and applies cross-modal attention for information transfer. Fused features, enhanced by segmentation and positional encodings, are decoded by an implicit network for HR prediction. This approach allows the model to ‘diversify’ its processing, integrating knowledge at various stages, from feature extraction to reconstruction.

3.3 Feature Extraction

Multi-modal MRI provides complementary tissue contrasts but often suffers from inconsistent spatial resolutions due to acquisition protocols. For example, T1w may be acquired at $40 \times 40 \times 20$, while T2w could be $40 \times 10 \times 40$. This spatial heterogeneity presents significant challenges for effective high-fidelity super-resolution.

To address this, our framework explicitly disentangles and exploits both the anatomical structures shared across modalities and the modality-specific details unique. Given paired T1w and T2w volumes \mathbf{X}_1 and \mathbf{X}_2 (each of shape $[B, 1, D, H, W]$), we employ two parallel encoders for each modality: 1) **Shared encoder** ($\text{Encoder}_m^{\text{shared}}$): Extracts features representing anatomical structures common to both modalities, enabling robust cross-modal guidance. 2) **Modality-specific encoder** ($\text{Encoder}_m^{\text{spec}}$): Captures unique contrasts and details essential for preserving modality-specific information during fusion and reconstruction.

Formally, for $m \in \{1, 2\}$ (T1w and T2w), the extracted features are

$$\mathbf{F}_m^{\text{shared}} = \text{Encoder}_m^{\text{shared}}(\mathbf{X}_m), \quad (2)$$

$$\mathbf{F}_m^{\text{spec}} = \text{Encoder}_m^{\text{spec}}(\mathbf{X}_m). \quad (3)$$

Due to the mismatch in spatial resolutions, all feature maps are upsampled to a unified high-resolution grid (e.g., $40 \times 40 \times 40$) using trilinear interpolation:

$$\tilde{\mathbf{F}}_m^{\text{shared}} = \text{Interp}(\mathbf{F}_m^{\text{shared}}), \quad (4)$$

$$\tilde{\mathbf{F}}_m^{\text{spec}} = \text{Interp}(\mathbf{F}_m^{\text{spec}}). \quad (5)$$

This upsampling ensures spatial alignment for subsequent attention and loss computations, enabling accurate voxel-wise information transfer.

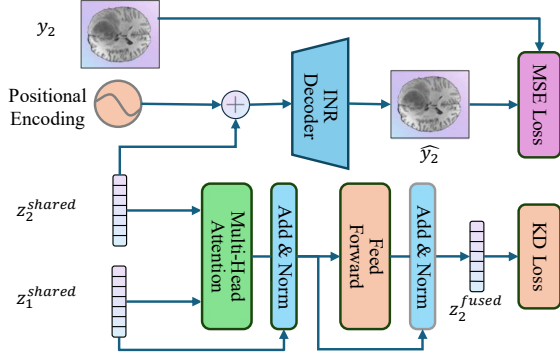


Figure 3: Illustration of the cross-modal attention-based knowledge distillation and T2w self-reconstruction loss. y_2 denotes the ground-truth T2w image, while \hat{y}_2 denotes the predicted T2w image.

3.4 Knowledge Distillation via Cross-Modal Attention

A core challenge in multi-modal super-resolution is how to effectively transfer the rich anatomical priors of the high-resolution modality (T1w) to guide the reconstruction of the low-resolution modality (T2w). To achieve this, we introduce a cross-modal attention mechanism that enables T2w’s shared features to dynamically attend to T1w’s shared features at each location in the unified high-resolution space.

This design is motivated by the observation that simple concatenation or addition of features is insufficient for capturing complex, spatially-varying correlations between modalities, especially under resolution mismatch. Cross-attention allows the model to learn spatially-adaptive, content-aware guidance from the teacher (T1w) to the student (T2w), enhancing the transfer of fine anatomical structures.

The attention-enhanced T2w shared feature is computed as:

$$\tilde{\mathbf{F}}_2^{\text{fused}} = \text{CrossAttn}(\tilde{\mathbf{F}}_2^{\text{shared}}, \tilde{\mathbf{F}}_1^{\text{shared}}), \quad (6)$$

where $\text{CrossAttn}(\cdot, \cdot)$ denotes a cross-attention block with T2w as query and T1w as key/value, operating voxel-wise after upsampling.

To facilitate supervision and ensure that the student branch (T2w) learns to mimic the teacher’s (T1w) anatomical encoding, we sample both the T1w shared features and the attention-fused T2w features at a set of high-resolution coordinates $\{\mathbf{p}_i\}_{i=1}^K$:

$$\mathbf{z}_1^{\text{shared}} = \text{GridSample}(\tilde{\mathbf{F}}_1^{\text{shared}}, \{\mathbf{p}_i\}), \quad (7)$$

$$\mathbf{z}_2^{\text{fused}} = \text{GridSample}(\tilde{\mathbf{F}}_2^{\text{fused}}, \{\mathbf{p}_i\}), \quad (8)$$

where $\text{GridSample}(\cdot, \cdot)$ denotes trilinear interpolation and $\mathbf{z}_1^{\text{shared}}, \mathbf{z}_2^{\text{fused}} \in \mathbb{R}^{B \times K \times C}$.

Based on the above, we establish a voxel-level knowledge distillation loss:

$$\mathcal{L}_{\text{KD}} = \frac{1}{BK} \sum_{b=1}^B \sum_{k=1}^K \left\| \mathbf{z}_2^{\text{fused},(b,k)} - \mathbf{z}_1^{\text{shared},(b,k)} \right\|_2^2. \quad (9)$$

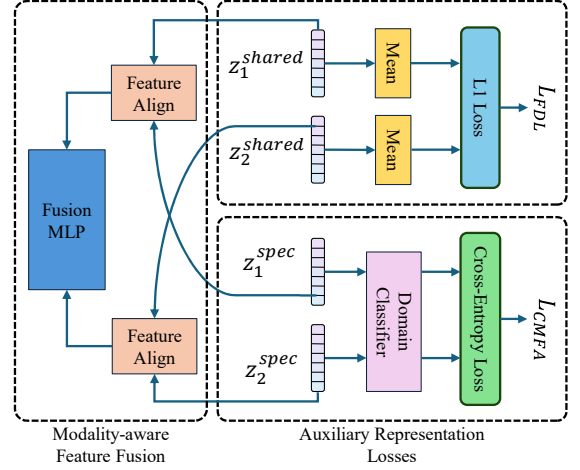


Figure 4: Workflow of auxiliary losses: CMFA aligns the mean of shared features across modalities via L1 loss, while FDL uses a classifier and cross-entropy loss to enforce modality discrimination on specific features.

This loss enforces that, at every spatial location, the T2w branch captures the anatomical structures encoded by T1w, thus enabling robust cross-modal guidance for ARSR.

In addition, to further enhance the representation learning for the target modality, we introduce a self-reconstruction loss for T2w. Specifically, the upsampled shared T2w features are sampled at the same set of coordinates and combined with positional encoding, then decoded to predict the high-resolution T2w intensity:

$$\mathbf{z}_2^{\text{shared}} = \text{GridSample}(\tilde{\mathbf{F}}_2^{\text{shared}}, \{\mathbf{p}_i\}). \quad (10)$$

The decoder predicts the intensity \hat{y}_2^{self} and the loss is defined as:

$$\mathcal{L}_{\text{T2Self}} = \frac{1}{BK} \sum_{b=1}^B \sum_{k=1}^K \left\| \hat{y}_2^{\text{self},(b,k)} - y_2^{(b,k)} \right\|_2^2, \quad (11)$$

where $y_2^{(b,k)}$ is the ground-truth T2w intensity at location \mathbf{p}_i .

The total objective for cross-modal knowledge transfer is a weighted sum of the two losses:

$$\mathcal{L}_{\text{KD_total}} = \lambda_{\text{KD}} \mathcal{L}_{\text{KD}} + \lambda_{\text{T2Self}} \mathcal{L}_{\text{T2Self}}, \quad (12)$$

where λ_{KD} and λ_{T2Self} are hyperparameters balancing the two terms.

By jointly optimizing these objectives, our framework enables the T2w branch to effectively absorb high-resolution anatomical priors from the T1w and maintain self-consistency, even in the presence of cross-modal misalignment, thereby significantly improving the quality and anatomical fidelity of the super-resolved outputs.

3.5 Multi-Modal Feature Fusion by Auxiliary Losses

After attention-based knowledge transfer, we further integrate the shared and modality-specific features of each modality to obtain discriminative, information-rich representations for downstream reconstruction.

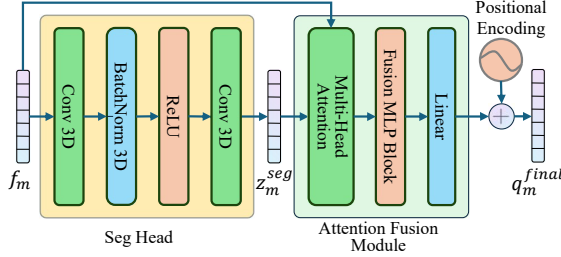


Figure 5: Workflow of segmentation-enhanced feature fusion and final implicit decoding.

Residual Feature Fusion. For each modality $m \in \{1, 2\}$, we sample both the upsampled shared and specific features at the target coordinates:

$$\mathbf{z}_m^{\text{shared}} = \begin{cases} \text{GridSample}(\tilde{\mathbf{F}}_1^{\text{shared}}, \{\mathbf{p}_i\}), & m = 1. \\ \text{GridSample}(\tilde{\mathbf{F}}_2^{\text{fused}}, \{\mathbf{p}_i\}), & m = 2. \end{cases} \quad (13)$$

$$\mathbf{z}_m^{\text{spec}} = \text{GridSample}(\tilde{\mathbf{F}}_m^{\text{spec}}, \{\mathbf{p}_i\}). \quad (14)$$

We then concatenate the sampled shared and specific features and project them through a multi-layer perceptron (MLP) with a residual connection:

$$\mathbf{h}_m = [\mathbf{z}_m^{\text{shared}}, \mathbf{z}_m^{\text{spec}}]. \quad (15)$$

$$\mathbf{f}_m = f_{\text{proj}}(\mathbf{h}_m) + \mathbf{z}_m^{\text{shared}}. \quad (16)$$

Here, the residual design preserves the core anatomical structure while allowing the network to flexibly integrate modality-specific cues.

Positional Encoding. To provide explicit spatial context, we compute positional encodings (Fourier features) for all target coordinates and concatenate them with the fused features:

$$\mathbf{q}_m = [\mathbf{f}_m, \mathbf{e}_m], \quad (17)$$

where $\mathbf{e}_m \in \mathbb{R}^{K \times d_e}$ is the positional encoding for modality m .

Auxiliary Losses. To further enhance feature consistency and discrimination, we introduce two auxiliary losses, as illustrated in Figure 4:

Cross-Modal Mean Feature Alignment Loss (CMFA). This loss encourages the mean shared features of both modalities to be close, promoting robust cross-modal alignment:

$$\mathcal{L}_{\text{CMFA}} = \|\text{Mean}(\mathbf{z}_1^{\text{shared}}) - \text{Mean}(\mathbf{z}_2^{\text{shared}})\|_1. \quad (18)$$

Feature Discrimination Loss (FDL, Cross-Entropy). This loss encourages the modality-specific features to be discriminative, facilitating downstream tasks such as modality classification and robust fusion:

$$\mathcal{L}_{\text{FDL}} = \text{CE}(f_{\text{cls}}(\mathbf{z}_1^{\text{spec}}), 0) + \text{CE}(f_{\text{cls}}(\mathbf{z}_2^{\text{spec}}), 1), \quad (19)$$

where f_{cls} is a lightweight classifier and 0, 1 are the modality labels for T1w and T2w, respectively.

The final representation \mathbf{q}_m is then ready for implicit decoding to predict high-resolution voxel intensities (details omitted here).

3.6 Segmentation-Enhanced Learning

Our framework adopts a multi-task learning strategy, jointly optimizing super-resolution and segmentation tasks with shared encoders. This joint training encourages the learned representations to be informative for both high-fidelity reconstruction and accurate anatomical delineation.

For each modality, the fused features \mathbf{f}_1 and \mathbf{f}_2 at query coordinates are obtained by integrating shared and specific features via residual MLP fusion, and then passed through segmentation heads to generate segmentation logits:

$$\mathbf{z}_1^{\text{seg}} = f_{\text{seg}}^1(\mathbf{f}_1), \quad (20)$$

$$\mathbf{z}_2^{\text{seg}} = f_{\text{seg}}^2(\mathbf{f}_2), \quad (21)$$

where f_{seg}^1 and f_{seg}^2 denote the segmentation heads for T1w and T2w, respectively.

To further enhance super-resolution, segmentation features are fused back with the original features by channel-wise concatenation and a fusion MLP:

$$\mathbf{h}_1^{\text{final}} = f_{\text{fusion}}^1([\mathbf{f}_1, \mathbf{z}_1^{\text{seg}}]), \quad (22)$$

$$\mathbf{h}_2^{\text{final}} = f_{\text{fusion}}^2([\mathbf{f}_2, \mathbf{z}_2^{\text{seg}}]), \quad (23)$$

where f_{fusion}^1 and f_{fusion}^2 are fusion MLPs for T1w and T2w, respectively.

Finally, the final features are concatenated with positional encodings for the implicit decoder:

$$\mathbf{q}_1^{\text{final}} = [\mathbf{h}_1^{\text{final}}, \mathbf{e}_1], \quad (24)$$

$$\mathbf{q}_2^{\text{final}} = [\mathbf{h}_2^{\text{final}}, \mathbf{e}_2], \quad (25)$$

where \mathbf{e}_1 and \mathbf{e}_2 are positional encodings for T1w and T2w, respectively. The resulting features are then fed into the implicit decoder to predict high-resolution voxel intensities.

The segmentation heads are supervised by a cross-entropy loss with respect to the ground-truth segmentation masks. The overall objective is a weighted sum of the super-resolution loss, segmentation loss, and auxiliary losses:

$$\mathcal{L} = \mathcal{L}_{\text{SR}} + \lambda_{\text{seg}} \mathcal{L}_{\text{seg}} + \lambda_{\text{aux}} \mathcal{L}_{\text{aux}}, \quad (26)$$

where λ_{seg} and λ_{aux} are weighting factors.

This design enables the model to leverage both dense image-level and anatomical supervision, leading to improved reconstruction fidelity, anatomical accuracy, and generalization.

4 Experiments

4.1 Datasets and Evaluation Metrics

To better simulate clinical MRI acquisition, we constructed our dataset from the BraTS collection. Due to T1w images are often acquired at higher spatial resolution than T2w images, and MRI data typically exhibit anisotropic resolution. We therefore downsampled T1w images along the z-axis to $240 \times 240 \times 80$ and T2w images along the y-axis to $240 \times 60 \times 160$, reflecting clinical acquisition protocols with different orientations for each modality. A total of 73 subjects with isotropic ground-truth scans were selected, split into 48 for training, 10 for validation, and 15 for testing. All

Method	PSNR \uparrow			SSIM \uparrow			LPIPS \downarrow		
	T1w	T2w	Avg	T1w	T2w	Avg	T1w	T2w	Avg
Trilinear	26.50	25.10	25.80	0.8700	0.8550	0.8625	0.0420	0.0480	0.0450
SMORE (Zhao et al. 2021)	29.20	27.80	28.50	0.9400	0.9250	0.9325	0.0280	0.0320	0.0300
I3Net (Song et al. 2024)	30.60	29.20	29.90	0.9550	0.9400	0.9475	0.0170	0.0210	0.0190
SAINT (Peng et al. 2020)	<u>31.50</u>	<u>30.10</u>	<u>30.80</u>	0.9520	0.9370	0.9445	0.0310	0.0350	0.0330
ArSSR (Wu et al. 2022)	30.01	28.58	29.30	0.9378	0.9318	0.9348	<u>0.0138</u>	<u>0.0185</u>	<u>0.0161</u>
SSMCSR [#] (McGinnis et al. 2023)	<u>31.50</u>	30.00	30.75	<u>0.9630</u>	<u>0.9480</u>	<u>0.9555</u>	0.0280	0.0320	0.0300
CycleINR* (Fang et al. 2024)	30.60	29.20	29.90	0.9490	0.9340	0.9415	0.0150	0.0190	0.0170
Nexus-INR (Ours)	33.75	32.25	33.00	0.9772	0.9566	0.9669	0.0038	0.0095	0.0067

Table 1: Comparison with state-of-the-art methods on the BraTS2020 test set. The best two results are highlighted in bold and underline. *: CycleINR results are from our own implementation according to the original paper due to unavailable code. #: SSMCSR is subject-specific and cannot be trained/evaluated on the whole dataset.

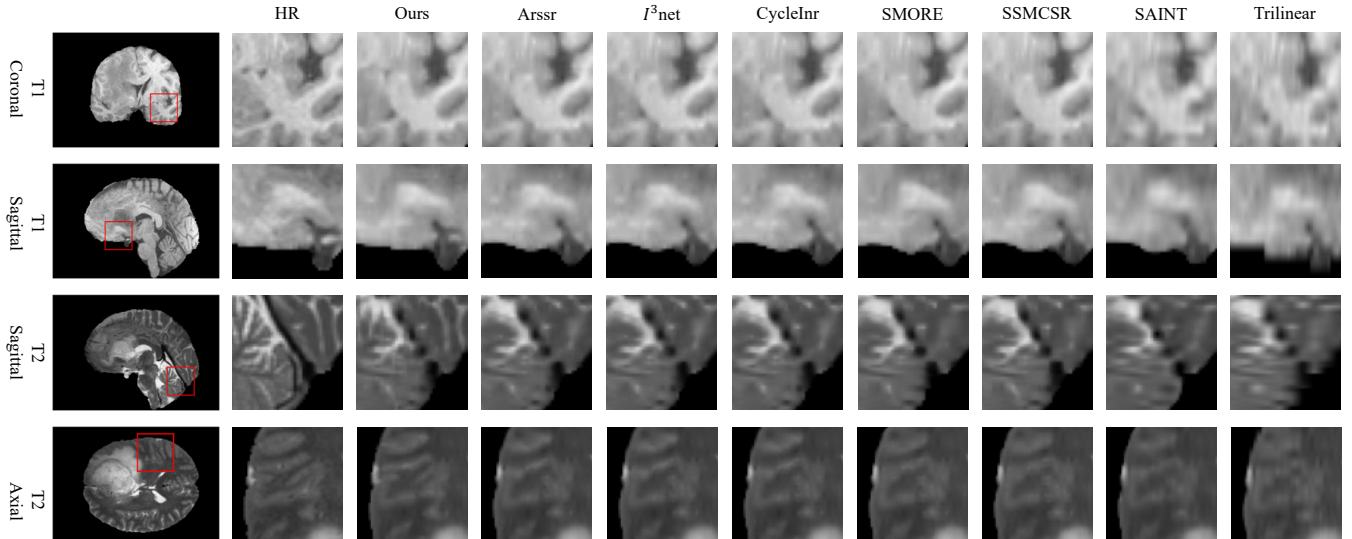


Figure 6: Visual comparison of super-resolved slices produced by different methods on the BraTS2020 test set. Our Nexus-INR achieves sharper boundaries and better anatomical fidelity compared to other state-of-the-art approaches.

images were normalized and zero-padded to $240 \times 240 \times 160$. T1w and T2w volumes were cropped into $40 \times 40 \times 20$ and $40 \times 10 \times 40$ patches, respectively, and only patches containing sufficient foreground were retained.

For evaluation, we report Peak Signal-to-Noise Ratio (PSNR), Structural Similarity Index Measure (SSIM), and Learned Perceptual Image Patch Similarity (LPIPS) to assess both fidelity and perceptual quality.

4.2 Implementation Details

All experiments are implemented in PyTorch and conducted on two NVIDIA RTX 4090 GPUs. The encoder adopts the RDN (Zhang et al. 2018) architecture (feature dimension 128), and the implicit decoder is a 4-layer MLP with 256 units per layer. We use the Adam optimizer with a learning rate of 1×10^{-4} and batch size 22. The total loss is a weighted sum of all task losses.

MRI volumes are normalized to zero mean and unit variance. Data augmentation includes random flipping and rotation. Model selection is based on the best validation PSNR, and all experiments are repeated with three random seeds for reproducibility. During inference, the model supports

arbitrary-resolution prediction by querying the implicit decoder with any desired coordinate grid.

4.3 Comparison with State-of-the-art Methods

We compare our Nexus-INR with several state-of-the-art (SOTA) methods on the BraTS2020 test set, where SMORE (Zhao et al. 2021), I3Net (Song et al. 2024), and SAINT (Peng et al. 2020) are CNN-based methods, while ArSSR (Wu et al. 2022), SSMCSR (McGinnis et al. 2023), and CycleINR (Fang et al. 2024) are INR-based methods. It should be noted that the results of CycleINR are from our own implementation according to the original paper, and the results of SSMCSR is subject-specific. Results of other methods are tested and calculated by ourselves.

As presented in Table 1, our Nexus-INR achieves the best performance on all metrics. Especially on the lower-resolution T2w modality, it outperforms all others by at least 2.15 PSNR points and leads in SSIM. It also significantly reduces LPIPS, showing remarkable gains in perceptual quality and detail recovery. Figure 6 shows representative super-resolved slices of T1w and T2w modalities by different methods. We can observe that our Nexus-INR more

Components				PSNR \uparrow			SSIM \uparrow			LPIPS \downarrow		
Baseline	MMF	KD-Attn	SEL	T1w	T2w	Avg	T1w	T2w	Avg	T1w	T2w	Avg
✓				30.01	28.58	29.30	0.9378	0.9318	0.9348	0.0138	0.0185	0.0161
✓	✓			33.72	29.71	31.72	0.9769	0.9324	0.9547	0.0040	0.0207	0.0124
✓	✓	✓		33.63	32.07	32.85	0.9764	0.9551	0.9657	0.0039	0.0111	0.0075
✓	✓	✓	✓	33.75	32.25	33.00	0.9772	0.9566	0.9669	0.0038	0.0095	0.0067

Table 2: Ablation study of Nexus-INR components on BraTS2020 (Nexus-INR = MMF + KD-Attn + SEL). MMF: Multi-Modal Fusion, KD-Attn: Cross-Modal Attention, SEL: Segmentation-Enhanced Learning.

Encoder	PSNR \uparrow	SSIM \uparrow	LPIPS \downarrow
SRResNet	33.12	0.9635	0.0084
ResCNN	32.85	0.9612	0.0091
RDN	33.75	0.9669	0.0067

Table 3: Comparison of different encoder backbones in Nexus-INR on the BraTS2020 test set.

INR Decoder	PSNR \uparrow	SSIM \uparrow	LPIPS \downarrow
SIREN	33.21	0.9639	0.0081
MLP	33.75	0.9669	0.0067

Table 4: Comparison of different INR decoders in Nexus-INR on the BraTS2020 test set.

faithfully restores brain structures and fine details, such as tissue boundaries and cortical features, especially in challenging T2w images. This shows our method is superior to other algorithms in both qualitative and quantitative evaluations of output images.

4.4 Ablation Analysis

We conduct ablation experiments by incrementally adding MMF, KD-Attn, and SEL modules to the baseline model, retraining under the same settings. As presented in Table 2, we can observe that each module incrementally improves PSNR, SSIM, and LPIPS, with KD-Attn notably boosting T2w performance. The full model achieves the best results, confirming the effectiveness of our design.

4.5 Impact of Encoder and Implicit Representation Choices

To further evaluate the flexibility and generalizability of our framework, we conduct additional experiments on the BraTS2020 test set by replacing the backbone encoder and INR decoder within Nexus-INR. For the encoder comparison, we evaluate three representative backbones: RDN, SRResNet (Ledig et al. 2017), and ResCNN (Du et al. 2020b). For the INR decoder comparison, we consider two popular implicit decoders: MLP and SIREN. All other experimental settings are kept consistent with the main experiments. As presented in Table 3 and Table 4, we can observe that our Nexus-INR demonstrates robust performance across different encoder and INR decoder choices, further verifying its versatility and compatibility with a variety of network designs.

Method	U-Net		TransUNet	
	Dice \uparrow	HD95 \downarrow	Dice \uparrow	HD95 \downarrow
Original LR	78.80	8.65	79.40	8.33
Trilinear	82.65	7.24	83.11	7.05
SMORE	85.72	6.58	86.09	6.31
I3Net	86.18	6.31	86.73	6.12
SAINT	86.35	6.24	86.98	6.05
ArSSR	87.02	5.90	87.41	5.64
SSMCSR [#]	87.18	5.84	87.52	5.61
CycleINR [*]	87.24	5.79	87.63	5.55
Nexus-INR (Ours)	88.92	5.03	88.97	4.82
Original HR	90.12	4.32	91.05	3.97

Table 5: Segmentation performance (Dice \uparrow , HD95 \downarrow) of U-Net and TransUNet on super-resolved images from different methods. *: CycleINR results are from our own implementation according to the original paper due to unavailable code. #: SSMCSR is subject-specific and cannot be trained/evaluated on the whole dataset.

4.6 Impact on Segmentation Task

To assess the effect of different super-resolution methods on downstream segmentation, we use a unified evaluation pipeline: first, each method is used to generate super-resolved images from low-resolution inputs; then, both a 3D U-Net and a TransUNet (Chen et al. 2021) are tested on these images for tumor segmentation. All segmentation models are tested under the same conditions to ensure a fair comparison. Segmentation performance is evaluated using the Dice similarity coefficient (Dice, higher is better) and the 95th percentile Hausdorff Distance (HD95, lower is better) on the BraTS2020 test set. As presented in Table 5, we can observe that our Nexus-INR achieves the best segmentation accuracy and boundary quality for both U-Net and TransUNet, demonstrating that our approach is also the most meaningful for downstream tasks.

Conclusion

In this paper, we propose Nexus-INR, a dual branch network for high-quality, adaptive-resolution medical image super-resolution. Nexus-INR integrates multi-modal fusion, cross-modal knowledge distillation, and segmentation-enhanced learning to leverage diverse knowledge to handle multi-modal images and provide more accurate data for downstream tasks. Experiments on the BraTS2020 dataset show that Nexus-INR outperforms state-of-the-art methods in both image quality and downstream segmentation performance.

References

- Cao, J.; Wang, Q.; Xian, Y.; Li, Y.; Ni, B.; Pi, Z.; Zhang, K.; Zhang, Y.; Timofte, R.; and Van Gool, L. 2023. Ciasor: Continuous implicit attention-in-attention network for arbitrary-scale image super-resolution. In *Proceedings of the IEEE/CVF Conference on Computer Vision and Pattern Recognition*, 1796–1807.
- Chen, J.; Lu, Y.; Yu, Q.; Luo, X.; Adeli, E.; Wang, Y.; Lu, L.; Yuille, A. L.; and Zhou, Y. 2021. Transunet: Transformers make strong encoders for medical image segmentation. *arXiv preprint arXiv:2102.04306*.
- Chen, W.; Wu, S.; Wang, S.; Li, Z.; Yang, J.; Yao, H.; Tian, Q.; and Song, X. 2025. Multi-contrast image super-resolution with deformable attention and neighborhood-based feature aggregation (DANCE): Applications in anatomic and metabolic MRI. *Medical Image Analysis*, 99: 103359.
- Chen, Y.; Liu, S.; and Wang, X. 2021. Learning continuous image representation with local implicit image function. In *Proceedings of the IEEE/CVF conference on computer vision and pattern recognition*, 8628–8638.
- Chen, Y.; and Wang, X. 2022. Transformers as meta-learners for implicit neural representations. In *European Conference on Computer Vision*, 170–187. Springer.
- Chen, Y.; Xie, Y.; Zhou, Z.; Shi, F.; Christodoulou, A. G.; and Li, D. 2018. Brain MRI super resolution using 3D deep densely connected neural networks. In *2018 IEEE 15th international symposium on biomedical imaging (ISBI 2018)*, 739–742. IEEE.
- Du, J.; He, Z.; Wang, L.; Gholipour, A.; Zhou, Z.; Chen, D.; and Jia, Y. 2020a. Super-resolution reconstruction of single anisotropic 3D MR images using residual convolutional neural network. *Neurocomputing*, 392: 209–220.
- Du, J.; He, Z.; Wang, L.; Gholipour, A.; Zhou, Z.; Chen, D.; and Jia, Y. 2020b. Super-resolution reconstruction of single anisotropic 3D MR images using residual convolutional neural network. *Neurocomputing*, 209–220.
- Ekanayake, M.; Chen, Z.; Egan, G.; Harandi, M.; and Chen, Z. 2025. SeCo-INR: Semantically Conditioned Implicit Neural Representations for Improved Medical Image Super-Resolution. In *2025 IEEE/CVF Winter Conference on Applications of Computer Vision (WACV)*, 117–126. IEEE.
- Fang, W.; Tang, Y.; Guo, H.; Yuan, M.; Mok, T. C.; Yan, K.; Yao, J.; Chen, X.; Liu, Z.; Lu, L.; et al. 2024. CycleINR: Cycle Implicit Neural Representation for Arbitrary-Scale Volumetric Super-Resolution of Medical Data. In *Proceedings of the IEEE/CVF Conference on Computer Vision and Pattern Recognition*, 11631–11641.
- Feng, C.-M.; Fu, H.; Yuan, S.; and Xu, Y. 2021. Multi-contrast MRI super-resolution via a multi-stage integration network. In *Medical Image Computing and Computer Assisted Intervention–MICCAI 2021: 24th International Conference, Strasbourg, France, September 27–October 1, 2021, Proceedings, Part VI* 24, 140–149. Springer.
- Feng, C.-M.; Yan, Y.; Yu, K.; Xu, Y.; Fu, H.; Yang, J.; and Shao, L. 2024. Exploring separable attention for multi-contrast MR image super-resolution. *IEEE Transactions on Neural Networks and Learning Systems*.
- He, X.; Wang, Y.; Zhao, S.; and Chen, X. 2023. Joint segmentation and classification of skin lesions via a multi-task learning convolutional neural network. *Expert Systems with Applications*, 230: 120174.
- Ledig, C.; Theis, L.; Huszar, F.; Caballero, J.; Cunningham, A.; Acosta, A.; Aitken, A.; Tejani, A.; Totz, J.; Wang, Z.; and Shi, W. 2017. Photo-Realistic Single Image Super-Resolution Using a Generative Adversarial Network. In *2017 IEEE Conference on Computer Vision and Pattern Recognition (CVPR)*.
- Lyu, Q.; Shan, H.; Steber, C.; Helis, C.; Whitlow, C.; Chan, M.; and Wang, G. 2020. Multi-contrast super-resolution MRI through a progressive network. *IEEE transactions on medical imaging*, 39(9): 2738–2749.
- McGinnis, J.; Shit, S.; Li, H. B.; Sideri-Lampretsa, V.; Graf, R.; Dannecker, M.; Pan, J.; Stolt-Ansó, N.; Mühlau, M.; Kirschke, J. S.; et al. 2023. Single-subject multi-contrast MRI super-resolution via implicit neural representations. In *International Conference on Medical Image Computing and Computer-Assisted Intervention*, 173–183. Springer.
- Peng, C.; Lin, W.-A.; Liao, H.; Chellappa, R.; and Zhou, S. K. 2020. Saint: spatially aware interpolation network for medical slice synthesis. In *Proceedings of the IEEE/CVF Conference on Computer Vision and Pattern Recognition*, 7750–7759.
- Pham, C.-H.; Ducournau, A.; Fablet, R.; and Rousseau, F. 2017. Brain MRI super-resolution using deep 3D convolutional networks. In *2017 IEEE 14th International Symposium on Biomedical Imaging (ISBI 2017)*, 197–200.
- Sitzmann, V.; Martel, J.; Bergman, A.; Lindell, D.; and Wetzstein, G. 2020. Implicit neural representations with periodic activation functions. *Advances in neural information processing systems*, 33: 7462–7473.
- Song, H.; Mao, X.; Yu, J.; Li, Q.; and Wang, Y. 2024. I³Net: Inter-Intra-Slice Interpolation Network for Medical Slice Synthesis. *IEEE Transactions on Medical Imaging*, 43(9): 3306–3318.
- Tancik, M.; Mildenhall, B.; Wang, T.; Schmidt, D.; Srinivasan, P. P.; Barron, J. T.; and Ng, R. 2021. Learned initializations for optimizing coordinate-based neural representations. In *Proceedings of the IEEE/CVF conference on computer vision and pattern recognition*, 2846–2855.
- Tancik, M.; Srinivasan, P.; Mildenhall, B.; Fridovich-Keil, S.; Raghavan, N.; Singhal, U.; Ramamoorthi, R.; Barron, J.; and Ng, R. 2020. Fourier features let networks learn high frequency functions in low dimensional domains. *Advances in neural information processing systems*, 33: 7537–7547.
- Wang, H.; Chen, Y.; Ma, C.; Avery, J.; Hull, L.; and Carneiro, G. 2023. Multi-modal learning with missing modality via shared-specific feature modelling. In *Proceedings of the IEEE/CVF Conference on Computer Vision and Pattern Recognition*, 15878–15887.
- Wang, L.; Li, D.; Zhu, Y.; Tian, L.; and Shan, Y. 2020. Dual Super-Resolution Learning for Semantic Segmentation. In

Proceedings of the IEEE/CVF Conference on Computer Vision and Pattern Recognition (CVPR).

Wu, Q.; Li, Y.; Sun, Y.; Zhou, Y.; Wei, H.; Yu, J.; and Zhang, Y. 2022. An arbitrary scale super-resolution approach for 3d mr images via implicit neural representation. *IEEE Journal of Biomedical and Health Informatics*, 27(2): 1004–1015.

Xiao, J.; Zhang, J.; Zou, D.; Zhang, X.; Ren, J.; and Wei, X. 2024. Semantic Segmentation Prior for Diffusion-Based Real-World Super-Resolution. *ArXiv*, abs/2412.02960.

Zhang, Y.; Tian, Y.; Kong, Y.; Zhong, B.; and Fu, Y. 2018. Residual Dense Network for Image Super-Resolution. In *2018 IEEE/CVF Conference on Computer Vision and Pattern Recognition*.

Zhao, C.; Dewey, B. E.; Pham, D. L.; Calabresi, P. A.; Reich, D. S.; and Prince, J. L. 2021. SMORE: A Self-Supervised Anti-Aliasing and Super-Resolution Algorithm for MRI Using Deep Learning. *IEEE Transactions on Medical Imaging*, 40(3): 805–817.